

Orbital Migration of Protoplanets in a Marginally Gravitationally Unstable Disk. II. Migration, Merging, and Ejection

Alan P. Boss

Earth & Planets Laboratory, Carnegie Institution for Science, 5241 Broad Branch Road, NW, Washington, DC 20015-1305

aboss@carnegiescience.edu

ABSTRACT

Protoplanets formed in a marginally gravitationally unstable (MGU) disk by either core accretion or disk instability will be subject to dynamical interactions with massive spiral arms, possibly resulting in inward or outward orbital migration, mergers with each other, or even outright ejection from the protoplanetary system. The latter process has been hypothesized as a possible formation scenario for the unexpectedly high frequency of unbound gas giant exoplanets (free floating planets, FFP). Previous calculations with the EDTONS fixed grid three dimensional (3D) hydrodynamics code found that protoplanets with masses from $0.01 M_{\oplus}$ to $3 M_{Jup}$ could undergo chaotic orbital evolutions in MGU disks for ~ 1000 yrs without undergoing monotonic inward or outward migration. Here the Enzo 2.5 adaptive mesh refinement (AMR) 3D hydrodynamics code is used to follow the formation and orbital evolution of protoplanets in MGU disks for up to 2000 yrs. The Enzo results confirm the basic disk fragmentation results of the EDTONS code, as well as the absence of monotonic inward or outward orbital migration. In addition, Enzo allows protoplanet mergers to occur, unlike EDTONS, resulting in a significant decrease in the number of protoplanets that survive for 1000 to 2000 yrs in the Enzo models. These models also imply that gas giants should be ejected frequently in MGU disks that fragment into large numbers of protoplanets, supporting ejection as a possible source mechanism for the observed FFPs.

Subject headings: planets and satellites: formation — protoplanetary disks

1. Introduction

Exoplanet demographics provide one of the ultimate arbiters of theories of exoplanet formation and evolution. Nielsen et al. (2019) used the GPI exoplanet survey to search

for planets with masses between 2 and 13 M_{Jup} and semimajor axes between 3 and 100 au, finding that the peak occurrence distance of giant planets was in the range of 1 to 10 au. Fulton et al. (2021) found the same peak occurrence distance of 1 to 10 au for the California Legacy Doppler velocities survey. Vigan et al. (2021) showed that the VLT SPHERES direct imaging survey of 150 stars detected 13 sub-stellar companions with masses between 1 and 75 M_{Jup} and semimajor axes between 5 and 300 au, finding that both core accretion (CA; Mizuno 1980) and disk instability (DI; Boss 1997) appeared necessary to explain the detections for the FGK stars in their sample.

Gas giant planets with orbital distances as large as 980 au have been discovered and studied (Wu et al. 2022). Forming giant exoplanets at such large distances by CA within the ~ 1 Myr lifetimes of the gaseous portion of protoplanetary disks is challenging (e.g., Chambers 2021), if not impossible. DI has the advantage of forming dense, self-gravitating clumps in a few orbital periods, relaxing the disk lifetime constraint for forming wide-orbit gas giants in situ (e.g., Boss 2011). Evidence for a gas giant protoplanet embedded in a spiral arm 93 au from AB Aurigae has been interpreted as an example of gas giant planet formation by DI (Currie et al. 2022; cf. Cadman et al. 2021; Zhou et al. 2022). DI has also been proposed as the source of the $\sim 10M_{Jup}$ exoplanet that orbits ~ 560 au from the massive binary β Centauri (Janson et al. 2021). Goda & Matsuo (2019) examined the demographics of 485 planetary systems and concluded that a hybrid theory of planet formation, involving both CA and DI, was needed to explain the exoplanet detections.

Miret-Roig et al. (2022) used a direct imaging survey coupled with Gaia and Hipparchos astrometry to search for unbound gas giant exoplanets in the Upper Scorpius and Ophiuchus young stellar association. Their survey yielded between 70 and 170 free floating planets (FFP), considerably more than might be expected to form as the tail end of the star formation process of molecular cloud core collapse and fragmentation, and suggested that ejection from unstable planetary systems might make a major contribution during the first 10 Myr. Gravitational microlensing has also found an abundance of likely FFPs, though these could also simply be bound planets with orbital distances greater than about 10 au (Mróz et al. 2020; Ryu et al. 2021). Vorobyov (2016) performed numerical simulations that supported the hypothesis that FFPs might be the result of planets ejected from massive MGU disks.

While exoplanet demographics reveal orbital characteristics at the present epoch, unless exoplanets do not undergo significant orbital evolution or migration following their formation, the present epoch orbital parameters are of limited usefulness in constraining their initial orbital distances. CA is the favored mechanism closer to the host star, as a result of shorter orbital periods, higher gas disk temperatures, and higher surface densities of solids, to name a few factors, while DI may be more effective at larger distances in suitably massive and cool

protoplanetary disks. For either CA or DI, a key question then becomes the extent to which protoplanets might migrate away from their birth orbits to their present epoch orbits.

As noted by Boss (2013), CA and DI both require giant protoplanets to form in the presence of disk gas. Theoretical work on protoplanetary orbital migration (e.g., Kley & Nelson 2012) usually focuses on protoplanets in disks where the disk mass is low enough that the disk self-gravity can be neglected, greatly simplifying the analysis. Protoplanet evolution in MGU disk models has been calculated by Boss (2005), Baruteau et al. (2011), and Michael et al. (2011). These studies each considered quite different initial conditions and found a wide range of outcomes, ranging from large-scale inward orbital migration to relatively little orbital migration. Boss (2013) studied the evolution of protoplanets formed by either CA and DI in MGU disks, noting that while a MGU disk is essential for formation by DI, even a giant planet formed by CA in a quiescent, non-MGU disk can experience a later phase of MGU disk interactions during the periodic FU Orionis outbursts experienced by young solar-type protostars, which are thought to involve a phase of disk gravitational instability that dumps disk mass onto the protostar (e.g., Zhu et al. 2010; Kuffmeier et al. 2018). Dunhill (2018) similarly suggested that giant planets formed by CA might undergo orbital migration during FU Orionis outbursts.

The Boss (2005, 2013) models were performed using the EDTONS three dimensional radiative hydrodynamics code, with a spherical coordinate grid that was fixed at moderate spatial resolution throughout the MGU disk evolutions. Virtual protoplanets were introduced at the beginning of each model to represent protoplanets as point sources of gravity, able to interact gravitationally with the disk and with each other and to accrete mass from the disk by Bondi-Hoyle accretion. Boss (2013) found that protoplanets with initial masses in the range from $0.01 M_{\oplus}$ to $3 M_{Jup}$ and initial orbital distances of 6 to 12 au in a MGU disk around a solar-mass protostar underwent chaotic orbital evolutions for ~ 1000 yr without undergoing the monotonic inward or outward migration that typically characterizes the Type I or Type II behavior of non-self-gravitating disk models (e.g., Kley & Nelson 2012).

The present models of protoplanet orbital evolution employ the Enzo 2.5 hydrodynamics code. Enzo is also a three dimensional (3D) code and uses Adaptive Mesh Refinement (AMR) in Cartesian coordinates to ensure that sharp gradients in fluid quantities such as shock fronts can be handled accurately. Enzo is able to replace exceptionally dense disk clumps with sink particles representing newly formed (by DI) protoplanets, which thereafter interact with each other and the disk while accreting disk gas, as do the virtual protoplanets in the Boss (2013) models. We thus seek here to use a completely different 3D hydro code to learn more about the possible outcomes for protoplanet orbital evolution in MGU disks, and to compare the results with the latest advances in exoplanet demographics.

2. Numerical Hydrodynamics Code

As noted by Boss & Keiser (2013), the Enzo 2.5 AMR code performs hydrodynamics (HD) using any one of three different algorithms (Collins et al. 2010; Bryan et al. 2014): (1) the piecewise parabolic method (PPM) of Colella & Woodward (1984), (2) the ZEUS method of Stone & Norman (1992), or (3) a Runge–Kutta third-order-based MUSCL (“monotone upstream-centered schemes for conservation laws”) algorithm based on the Godunov (1959) shock-handling HD method. Enzo is designed for handling strong shock fronts by solving the Riemann problem (e.g., Godunov 1959) for discontinuous solutions of a fluid quantity that should be conserved. The PPM option was used in the current models as a result of the testing on mass and angular momentum conservation performed with Enzo 2.0 by Boss & Keiser (2013), who found that PPM was better able to conserve mass and angular momentum during the collapse of a rotating isothermal cloud core (Boss & Bodenheimer 1979) than either ZEUS or MUSCL. Enzo is designed for parallel processing on high performance clusters (HPC), but when run on a single, dedicated 32-core node of the Carnegie memex HPC, a typical model still required 7 months of continuous computation to evolve for $\sim 10^3$ yrs of model time.

The Enzo 2.5 models were initialized on a 3D Cartesian grid with 32 top grid points in each direction. A maximum of 7 levels of refinement was used, with a factor of two refinement occurring for each level, so that the maximum possible effective grid resolution was $2^7 = 128$ times higher than the initial resolution of 32^3 , i.e., 4096^3 . The models with 7 levels needed an increase in the number of cell buffer zones (NumberBufferZones) to 3 from the default value of 1, which was used for the lower levels of refinement, in order to maintain reasonable time steps. Grid refinement was performed whenever necessary to ensure that the Jeans length constraint (e.g., Truelove et al. 1997; Boss et al. 2000) was satisfied by a factor of 4 for cells with a density at least eight times the initial density. Periodic boundary conditions were applied on each face of the grid cubic box, with each side either 60 au or 120 au in length. A point source of external gravity was used to represent a $1 M_{\oplus}$ protostar at the center of the grid. The maximum number of Green’s functions used to calculate the gravitational potential was 10. The time step typically used was 0.15 of the limiting Courant time step. The results were analyzed with the yt astrophysical analysis and visualization toolkit (Turk et al. 2011).

Following Boss & Keiser (2014), we used the Enzo 2.2 sink particle coding described by Wang et al. (2010). Sink particles are created in grid cells that have already been refined to the maximum extent permitted by the specified number of levels of grid refinement, but where the gas density still exceeds that consistent with the Jeans length criterion for avoiding spurious fragmentation (Truelove et al. 1997; Boss et al. 2000). As described by

Boss & Keiser (2014), sink particles accrete gas from their host cells at the modified Bondi-Hoyle accretion rate proposed by Ruffert (1994). Two parameters control the conditions under which sink particles can be merged together: the merging mass (`SinkMergeMass`) and the merging distance (`SinkMergeDistance`). The former of these two parameters is used to divide the sink particles into either large or small particles. Particles with less mass than `SinkMergeMass` are first subjected to being combined with any large particles that are located within the `SinkMergeDistance`. Any surviving small particles after this first step are then merged with any other small particles within the `SinkMergeDistance`. The merging process is performed in such a way as to ensure conservation of mass and linear momentum. Boss & Keiser (2014) found that their results for collapse and fragmentation of magnetic molecular cloud cores were not particularly sensitive to the choice of these two key parameters with regard to the tendency of the cores to undergo fragmentation into multiple protostar systems. The current paper uses the Wang et al. (2010) sink particle coding with the `SinkMergeMass` set equal to $0.01 M_{Jup}$ and the `SinkMergeDistance` set equal to 0.1 au, appropriate values for studying gas giant protoplanets in a 120 au-size region. Sink creation was only allowed for cells with densities exceeding the values listed in Table 1 (`DensThresh` in code units in the `sink_maker.C` subroutine). These densities were chosen to be low enough that sinks do form in the models, as the point of the present models was to study the orbital evolution of sink particles representing protoplanets in MGU disks rather than to study the precise physics of DI-induced fragmentation and clump formation in such disks (e.g., Boss 2021a,b).

The sink particles used in the Enzo models are similar to the virtual protoplanets (VPs) used in the EDTONS models: both are introduced in regions of density maxima and are intended to represent gravitationally bound clumps of disk gas that will contract to form gaseous protoplanets, as they orbit in the disk around the central protostar, interacting gravitationally with each other and the disk gas, even as they accrete more disk gas. There are several differences, however. Sink particles are created automatically by Enzo following the criteria noted above, sink particles with close encounters can be merged together, and sink particles that encounter a grid boundary reappear on the opposite boundary as a result of the periodic boundary conditions. VPs, on the other hand, are inserted when a density maximum exceeds the Jeans length or Toomre length criteria (Nelson 2006; Boss 2021a,b) for the current grid spatial resolution. VPs may undergo close encounters with each other but do not suffer mergers. VPs that strike either the inner or outer grid boundary are removed from the calculation.

While it would be desirable to compare flux-limited diffusion (FLD) approximation radiative hydrodynamic models from the EDTONS code with FLD radiative hydrodynamic models calculated by Enzo, the FLD routines available in Enzo are limited to non-local thermodynamic equilibrium (non-LTE), as Enzo was developed primarily for cosmological

simulations, whereas EDTONS assumes LTE. As a result, we are limited to using a simpler approach to handling the disk thermodynamics with the Enzo code. Boss (1998) showed that disk fragmentation could occur for strongly gravitationally unstable disks with either locally isothermal or locally adiabatic thermodynamics, using disk gas adiabatic exponents ranging from $\gamma = 1$ (purely isothermal) to $\gamma = 7/5$, which is appropriate for molecular hydrogen. Given that disks are subject to compressional heating, $\gamma = 1$ is not strictly correct, and given that disks that are optically thick at their midplanes can cool from their surfaces, $\gamma = 7/5$ is not strictly correct either. The physically correct behavior presumably lies somewhere in the middle of these two extremes.

Radiative cooling in optically thin regions was employed in the Enzo models, with a critical density for cooling of $10^{-13} \text{ g cm}^{-3}$; regions with densities above this critical value had the cooling rate decreased proportionally. This critical density was chosen because that is the disk midplane density where the dust grain opacity produces optical depths of order unity (e.g., Boss 1986). The cooling rates were modified from the default values in *cool_rates.in* to rates consistent with molecular line cooling in optically thin regions (Boss et al. 2010; Neufeld & Kaufman 1993). Because Enzo PPM hydrodynamics involves a Riemann solver that cannot be purely isothermal, i.e., γ cannot equal unity, the adiabatic index for the disk gas was taken to be $\gamma = 1.001$, appropriate for a nearly isothermal, but still adiabatic equation of state for an ideal gas. Test runs were computed for 100 yrs of evolution with both $\gamma = 7/5$ and $\gamma = 5/3$, but in both cases Enzo produced midplane disk temperatures that were over 10^4 K, whereas the initial disk had a maximum midplane temperature of 1500 K. The test runs with $\gamma = 1.001$ produced the expected maximum temperatures of ~ 1500 K, and hence $\gamma = 1.001$ was adopted for the models presented here. The resulting temperature distributions were also affected by the assumption of radiative cooling; spiral features in the midplane temperature distribution accompanied spiral features in the midplane density distribution, as is to be expected. Finally, the mean molecular weight of the gas was effectively taken to be $\mu = 2.4$, appropriate for a solar composition mixture of molecular hydrogen and helium.

3. Initial Conditions

Table 1 lists the models with variations in the number of levels of grid refinement, the outer disk and envelope temperatures, initial minimum value of the Toomre (1964) Q parameter, disk radius, calculational grid box size, and critical density for sink particle creation. A 60 au box size was used for the 20 au and 30 au radius disks, while a 120 au box size was used for 60 au radius disks, in order to give the disks sufficient room to evolve and

expand by the outward transport of angular momentum through gravitational interactions with the spiral arms and clumps. In the number of levels column, 34 means the model was initially run with 3 levels and then a fourth level of refinement was added.

The initial disks are based on the model HR disk from Boss (2001), with an outer disk temperature of 40 K and and disk envelope temperature of 50 K, which has been used as a standard initial model for many of the author’s disk instability models (e.g., Boss 2021a,b). Model HR has an initial minimum Toomre $Q \approx 1.3$, implying marginal stability to the growth of rings and spiral arms. The model HR initial disk has a mass of $0.091 M_{\odot}$ within an inner radius of 4 au and an outer radius of 20 au and orbits a $1 M_{\odot}$ central protostar. The Enzo models have have masses of $0.102 M_{\odot}$ for 20 au outer radius disks, slightly higher than in model HR because the Enzo models extend inward to 1 au, $0.142 M_{\odot}$ for 30 au outer radius disks, and $0.210 M_{\odot}$ for 60 au outer radius disks. The same disk density power-law-like Keplerian structure as in Boss (2001) is used for all of the models, with the structure being terminated at 20 au, 30 au, or 60 au. Figures 1 and 2 show cross sections of the initial disk density distribution for the 20 au disks, both parallel and perpendicular (i.e., disk midplane) to the disk rotation axis.

4. Results

Figure 3 shows the intermediate results for two of the four models that have the identical initial disk configuration (20 au radius) as the Boss (2001) model HR, depicted at the same time (190 yrs of evolution) as the same initial disk model (fldA) in Boss (2021b, cf. Figure 2a). Figure 3 shows that both of these models (3-1K-20 and 6-1K-20) rapidly evolved into a configuration of multiple spiral arms interspersed with dense clumps, as expected for a marginally gravitationally unstable disk. Also as expected, the degree of fragmentation and clump formation increases as the numerical grid resolution increases from 3 to 6 levels. When sink particles are allowed to form, the number of sink particles similarly increases as the resolution is improved. While the background disk looks quite similar for model 3-1K-20 with or without sink particles (Figure 3a,c), there is a clear difference in the case of model 6-1K-20 (Figure 3b,d), where the background disk has become perturbed into a prolate configuration due to the formation of a massive ($\sim 20M_{Jup}$) secondary companion (at one o’clock), with its own circumplanetary disk and tertiary companion, whose combined tidal forces have evidently distorted the disk’s overall appearance. Model fldA of Boss (2021b) had fragmented into a five clumps and three virtual protoplanets (i.e., sink particles) by 189 yrs, for a total of eight, considerably more than formed in the present model 3-1K-20, but not as many as in model 6-1K-20, suggesting that even with the quadrupled spatial

resolution of the Boss (2021b) EDTONS models, the adaptive mesh refinement feature of Enzo results in significantly improved numerical spatial resolution of the disk instability and fragmentation. Confirmation of the formation of long-lived fragments in the model HR disk (Boss 2001, 2021b) with the completely different hydrodynamical method used here provides strong support for the viability of the disk instability mechanism for the formation of gas giant protoplanets and higher mass companions.

Figure 4 displays the results after 2000 yrs for the Enzo models in Figure 3. The EDTONS model fldA in Boss (2021b) was stopped after only 189 yrs of evolution, but even still required over 4 years of computation on a single core of a node on memex, a Carnegie Institution computer cluster. EDTONS is based on code initially written in the late 1970s and is not parallelized. Enzo, in contrast, is a modern code designed to run on parallel processing systems like memex, and as a result the Enzo models can be computed much farther in time. Even still, model 3-1K-20 required one week to run for 2000 yrs of model time on a dedicated single memex node with 28 cores, while model 6-1K-20 required one year to run 2000 yrs on a dedicated 28-core node. Three dimensional hydrodynamics at high spatial resolution is computationally expensive, even when a parallelized code is employed.

Figure 4 shows that the evolution of these two models diverged considerably following the early fragmentation phase depicted in Figure 3. The two sink particles evident in Figure 4a have masses of $\sim 2M_{Jup}$ and $\sim 0.6M_{Jup}$, with a total gas disk mass of $\sim 99M_{Jup}$, while the 13-odd sink particles in Figure 4b have masses ranging from $\sim 0.2M_{Jup}$ to $\sim 23M_{Jup}$, for a total sink particle mass of $\sim 96M_{Jup}$, leaving a disk gas mass of only $\sim 5M_{Jup}$. Clearly, the final disk mass in model 3-1K-20 far outweighs the mass of the sink particles, and as a result the particles are unable to open gaps in the disk, though the disk has expanded outward to a radius of about 30 au as a result of the transport of disk mass and angular momentum outward, caused by the strong spiral arms evident in Figure 3a,c. The fact that sink particle formation has been so efficient in model 6-1K-20, with the total particle mass some 20 times larger than the disk mass, means that the particles rule the evolution and are able to clear out a distinct inner gap, centered on about 5 au (Figure 4b). In model 6-1K-20, the sink particles gained the bulk of the disk’s mass and angular momentum, so that the disk is not able to expand beyond its initial radius of 20 au. Three sink particles were accelerated to speeds high enough at their orbital location to be ejected altogether from the system, but because of the periodic boundary conditions imposed on the calculations by the Enzo self-gravity solver, these ejectable particles were returned to the system and underwent further interactions with the sink particles and disk gas.

Table 2 gives the maximum number of sink particles formed for all the models, as well as the number surviving at the end of the run. Table 2 shows that the maximum number of

sinks formed decreases as the initial disk gas temperature is increased, as this results in an increase in the Toomre minimum Q value (Table 1), i.e., in greater stability to the growth of rings and spiral arms, and hence to fragmentation and sink particle formation. By the time that the disk temperature is increased to 160 K, disk fragmentation is completely stifled in the Enzo models, consistent with the flux-limited diffusion approximation models of Boss (2021b), where fragmentation ceased for a minimum Toomre Q greater than 2.2.

Models 6-2K-30 and 7-2K-30 did not form sink particles, unlike the otherwise identical, but lower resolutions models 3-2K-30, 4-2K-30, and 5-2K-30, because this sequence used a fixed critical density for sink particle formation of 10^{-9} g cm $^{-3}$. That choice meant that the dense clumps formed in the two higher resolution models could always be resolved with more grid levels and finer spatial resolution, thereby preventing the clumps from exceeding the critical density required for sink particle formation, at least during the limited amount of model time that the 6- and 7-level models were able to be evolved (326 and 340 yrs, respectively). Small time steps prevented these two models from being evolved farther in time. Figure 5 shows these two models at their final times, showing that the spiral arms and nascent clumps become more distinct as the number of grid levels is increased, as expected when approaching the continuum limit of infinite spatial resolution.

Table 2 also lists the number of sink particles mergers, where $N_{merged-sinks} = N_{max-sinks} - N_{final-sinks}$, and the number of times that a sink particle would have been ejected if periodic boundary conditions were not required. Table 2 shows that mergers of sink particles are quite common in all of the models that formed sink particles, and evidently are responsible for much of the gain in mass of the particles, along with the ongoing accretion of disk gas, given that the number of mergers is usually comparable to, or far greater than, the final number of sink particles. The value $N_{escaped-sinks}$ can be quite large due to the sink particles' inability to escape the system; often the same particle bounces in and out in orbital radius and achieves escape velocity multiple times. Achieving the escape velocity usually occurs for particle orbital distances of 30 au to 40 au, but can also occur from 10 au to 20 au in the more unstable disks (e.g., 5-1K-20, 6-1K-20). The large numbers of escape episodes in the latter two models are clearly solely a result of the periodic boundary conditions, but they do indicate that ejected protoplanets are to be expected as a natural outcome of a phase of gas disk gravitational instability. Table 2 suggests that such a phase of protoplanetary disk evolution should result in the ejection of several gas giant protoplanets.

Figure 6 presents all of the sink particle masses and distances from the central star at the final times for the models. These distances correspond to observed separations in the absence of any other knowledge of the orbital parameters, i.e., the semimajor axis and eccentricity. The final masses range from $\sim 0.1M_{Jup}$ to $\sim 100M_{Jup}$, i.e., sub-Jupiters to

brown dwarfs and late M dwarf stars. Separations range from inside 1 au to over 30 au. Ejected particles would be at much larger distances, were ejection permitted.

Figure 6 shows that the black dots, representing the 20 au radius disks, tend to have higher masses ($> 10M_{Jup}$) inside 10 au than the blue dots, representing the 60 au radius disks, which tend to have lower masses ($< 1M_{Jup}$) inside 10 au. This outcome is the result of the 20 au radius disks all starting their evolutions from considerably more gravitationally unstable initial states, i.e., Toomre $Q_{minimum} = 1.3$ than the 60 au radius disks, with initial Toomre $Q_{minimum} = 1.9$ or 2.2. The 20 au radius models thus generally form more massive sink particles, as would be expected.

Figure 7 shows the sink particle masses as a function of the orbital semimajor axis at the final times for the models, while Figure 8 depicts these properties for the known exoplanets on the same scales. Figure 3b shows that fragmenting dense clumps appear between about 5 au and 20 au, which is the same distance range as most of the sink particles in Figure 7; only a few have migrated inside 1 au, and only a few orbit beyond about 20 au. Clearly the present models produce a goodly number of cool gas giants and brown dwarfs, but do not lend support for the formation and inward migration of the numerous hot and warm exoplanets evident in Figure 8: little evidence for monotonic inward orbital migration is seen. This result is consistent with the EDTONS models of Boss (2013).

Finally, Figure 9 shows the sink particle masses as a function of the orbital eccentricity at the final times for the models, while Figure 10 depicts these properties for the known exoplanets on the same scales. The present models show that the processes studied here of fragmentation, mergers, chaotic orbits, and ejections result in the observed wide range of eccentricities, though not the presumably tidally damped, near-zero eccentricities of the hot Jupiters.

5. Discussion

Drass et al. (2016) showed that the initial mass function in the Orion nebula cloud has two peaks, one at $0.25 M_{\odot}$ and another at $0.025 M_{\odot}$, and suggested that the latter peak was composed of brown dwarfs and isolated planetary-mass objects that had been ejected from circumstellar disks or multiple star systems. The large number of attempted ejections in the Enzo models that are listed in Table 2 fully support this hypothesis.

Feng et al. (2022) combined high-precision Doppler velocity data with Gaia and Hipparcos astrometry to constrain the masses and orbital parameters of 167 sub-stellar companions to nearby stars. Their Figure 3 shows that these 167 companions fully populate a parameter

space ranging from semimajor axes of ~ 2 au to ~ 40 au, with masses from $\sim 4M_{Jup}$ to $\sim 100M_{Jup}$, much like the upper right quadrant of Figure 7. Their Figure 3 also shows orbital eccentricities varying from 0 to 0.75, again in basic agreement with the range evident in the present models in Figure 9. These Enzo models suggest a unified formation mechanism of the 167 sub-stellar companions studied by Feng et al. (2022): fragmentation of MGU disks.

Galvagni et al. (2012) used a smoothed particle hydrodynamics (SPH) code to study clumps formed at ~ 100 au in a MGU disk, finding that the clumps could contract and heat up enough to begin molecular hydrogen dissociation, resulting in a dynamical collapse phase that can ensure their survival to tidal forces. Their results showed that this collapse phase could occur within $\sim 10^3$ yrs, shorter than the evolution times of the models considered here (Table 2), justifying the replacement of dense clumps with Enzo sink particles or EDTONS virtual protoplanets (e.g., Boss 2005, 2013).

Lichtenberg & Schleicher (2015) used Enzo to study fragments formed by the disk instability process in isothermal disks, but did not employ sink particles or radiative transfer effects, finding that the clumps formed were all lost by inward migration combined with the tidal force of the protostar. Stamatellos (2015) used a SPH code to study disks with radii of 100 au and high Toomre Q values. Planets inserted at 50 au either migrated inward or outward over 2×10^4 yrs, depending on whether they were allowed to gain mass or not, respectively.

Hall et al. (2017) used an SPH code to study the identification and interactions of disk fragments composed of clumps of SPH particles that formed from the fragmentation of a $0.25M_{\odot}$ disk of radius 100 au around a $1M_{\odot}$ protostar. Their models showed that fragment-fragment interactions early in the evolutions led to scattering of fragments to larger semi-major axes, as large as 250 au, and to increased eccentricities, as high as 0.7. While the periodic boundary conditions used in the present models preclude an assessment of the final semi-major axes after close encounters, the fact that the sink particle velocities were often sufficiently high to predict ejection from the system is consistent with the Hall et al. (2017) results showing efficient scattering outward (cf., Table 2). The eccentricity pumping found by Hall et al. (2017) is similarly consistent with that found in the present models (cf. Figure 9).

Hall et al. (2017) also studied tidal downsizing and disruption of fragments that ventured too close to the tidal forces of the central protostar, finding that more clumps were destroyed by tidal disruption than by disappearing in a merger event. Tidal downsizing was proposed by Nayakshin (2010, 2017) as a means for forming inner rocky worlds from gas giants formed in a disk instability, following the formation of rocky inner cores by the sedimentation of dust grains and pebbles to the center of the giant gaseous protoplanet (Boss

1997). Tidal downsizing remains as a creative means to form inner rocky worlds as a result of a gravitationally unstable gas disk. The present sink particle models, as well as the virtual protoplanet models of the EDTONS code, do not allow tidal downsizing to occur, though implicitly the loss of virtual protoplanets that hit the inner disk boundary in EDTONS code calculations could be considered the equivalent of the loss of gas giant protoplanets by tidal disruption. Modeling the interior structure and thermal evolution of slowly contracting gas giant protoplanets is a future challenge for these types of models, and tidal disruption could result in the loss of sink particles that pass close to the central protostar, though it can be seen in Figure 6 that few sink particles passed inside 1 au.

Fletcher et al. (2019) performed a code comparison study of the orbital migration of protoplanets inserted at 120 au in disks of 300 au radius, finding that protoplanets of $2 M_{Jup}$ migrated inward to ~ 40 au to ~ 60 au within $\sim 10^4$ yr. These code comparisons differ considerably from the present models, as only single protoplanets were injected, the disks used a $\gamma = 7/5$ adiabatic index, and the disks were gravitationally stable everywhere, with Toomre $Q \geq 2$. As a result, the evolutions did not undergo the chaotic evolutions of the present models, where the MGU disk produces strong spiral arms that interact with the numerous protoplanets that formed near the outset.

Finally, Rowther & Meru (2020) used a SPH code to study planet survival in self-gravitating disks. They found that a fixed-mass planet with a range of masses would migrate inward in the cool outer regions of their disks, but that this migration was halted once the planet reached the warm inner disk. In their models, a single planet at a time is embedded in a disk with a mild spiral arm structure. Compared to the multiple clumps, sink particles, and strong spiral arms that form and interact in the present models (e.g., Figure 3), it is clear that the Rowther & Meru (2020) planets do not undergo the chaotic orbital motions experienced by the Enzo models here (or the EDTONS models of Boss 2013), which prevent monotonic orbital migration.

6. Conclusions

The use of a completely different three dimensional hydrodynamical code (Enzo 2.5), with a completely different method for handling nascent protoplanets (sink particles), has produced results in good agreement with those obtained by the EDTONS code and the virtual protoplanet method (Boss 2005). Both codes agree that with high spatial resolution, the standard model HR disk (Boss 2001) fragments rapidly into multiple dense clumps and strong spiral arms. Both codes agree that when these clumps are replaced with particles that can accrete mass from the disk, the particles grow in mass and can orbit chaotically for 1000

yrs to 2000 yrs without suffering monotonic inward or outward orbital migration. In addition, the Enzo models show that the protoplanets have a high probability of close encounters with each other, leading either to mergers, or to being ejected from the protoplanetary system. Comparisons with the observational data on exoplanet demographics and FFPs suggest that gas disk gravitational instabilities have an important role to play in explaining the formation of sub-stellar companions with a wide range of masses and orbital distances.

I thank Sean Raymond for discussions about FFPs and Floyd Fayton for his invaluable assistance with the memex cluster. I also thank the reviewer for providing several suggestions for improving the manuscript. The computations were performed on the Carnegie Institution memex computer cluster (hpc.carnegiescience.edu) with the support of the Carnegie Scientific Computing Committee. The computations were performed using the Enzo code originally developed by the Laboratory for Computational Astrophysics at the University of California San Diego and now available at <https://enzo-project.org/>.

REFERENCES

- Baruteau, C., Meri, F., & Paadekooper, S.-J. 2011, MNRAS, 416, 1971
- Boss, A. P. 1986, ApJS, 62, 519
- Boss, A. P. 1997, Sci, 276, 1836
- Boss, A. P. 1998, ApJ, 503, 923
- Boss, A. P. 2001, ApJ, 563, 367
- Boss, A. P. 2005, ApJ, 629, 535
- Boss, A. P. 2011, ApJ, 731, 74
- Boss, A. P. 2013, ApJ, 764, 194
- Boss, A. P. 2021a, ApJ, 911, 146
- Boss, A. P. 2021b, ApJ, 923, 93
- Boss, A. P., & Bodenheimer, P. 1979, ApJ, 234, 289
- Boss, A. P., Fisher, R. T., Klein, R. I., & McKee, C. F. 2000, ApJ, 528, 325
- Boss, A. P., & Keiser, S. A. 2013, ApJ, 764, 136
- Boss, A. P., & Keiser, S. A. 2014, ApJ, 794, 44
- Boss, A. P., Keiser, S. A., Ipatov, S. I., Myhill, E. A., & Vanhala, H. A. T. 2010, ApJ, 708, 1268

- Bryan, G. L., Norman, M. L., O’shea, B. W., et al. 2014, *ApJS*, 211, 19
- Cadman, J., Rice, K., & Hall, C. 2021, *MNRAS*, 504, 2877
- Chambers, J. E. 2021, *ApJ*, 914, 102
- Colella, P., & Woodward, P. R. 1984, *JCoPh*, 54, 174
- Collins, D. C., Padoan, P., Norman, M. L., & Xu, H. 2011, *ApJ*, 731, 59
- Currie, T., Lawson, K., Schneider, G., et al. 2022, *Nature Astronomy*, April 4
- Drass, H., Haas, M., Chini, R., et al. 2016, *MNRAS*, 461, 1734
- Dunhill, A. C. 2018, *MNRAS*, 478, 3438
- Feng, F., Butler, R. P., Vogt, S. S., et al. 2022, *ApJSS*, 262, 21
- Fletcher, M., Nayakshin, S., Stamatellos, D., et al. 2019, *MNRAS*, 486, 4398
- Fulton, B. J., Rosenthal, L. J., Hirsch, L. A., et al. 2021, *ApJSS*, 255, 14
- Galvagni, M., Hayfield, T., Boley, A., et al. 2012, *MNRAS*, 427, 1725
- Goda, S., & Matsuo, T. 2019, *ApJ*, 876, 23
- Godunov, S. K. 1959, *Matematicheskii Sbornik*, 47, 271
- Hall, C., Forgan, D., & Rice, K. 2017, *MNRAS*, 470, 2517.
- Janson, M., Gratton, R., Rodet, L., et al. 2021, *Nature*, 600, 231
- Kley, W., & Nelson, R. P. 2012, *ARA&A*
- Kuffmeier, M., Frimann, S., Jensen, S. S., & Haugbolle, T. 2018, *MNRAS*, 475, 2642
- Lichtenberg, T., & Schleicher, D. R. G. 2015, *A&A*, 579, A32
- Michael, S., Durisen, R. H., & Boley, A. C. 2011, *ApJL*, 737, L42
- Miret-Roig, N., Bouy, H., Raymond, S. N., et al. 2022, *Nature Astronomy*, 6, 89
- Mizuno, H. 1980, *Prog Theor Phys*, 64, 544
- Mróz, P., Poleski, R., Han, C., et al. 2020, *AJ*, 159, 262
- Nayakshin, S. 2010, *MNRAS*, 408, L36
- Nayakshin, S. 2017, *PASA*, 34, e002
- Neufeld, D. A., & Kaufman, M. J. 1993, *ApJ*, 418, 263
- Nelson, A. F. 2006, *MNRAS*, 373, 1039
- Nielsen, E. L., De Rosa, R. J., Macintosh, B., et al. 2019, *AJ*, 158, 13
- Rowther, S., & Meru, F. 2020, *MNRAS*, 496, 1598

- Ruffert, M. 1994, *ApJ*, 427, 342
- Ryu, Y.-H., Chung, S.-J., Jung, K. L., et al. 2021, *AJ*, 161,126
- Stamatellos, D. 2015, *ApJL*, 810, L11
- Stone, J. M., & Norman, M. L. 1992, *ApJS*, 80, 753
- Toomre, A. 1964, *ApJ*, 139, 1217
- Truelove, J. K., Klein, R. I., McKee, C. F., et al. 1997, *ApJL*, 489, L179
- Turk, M. J., Smith, B. D., Oishi, J. S., et al. 2011, *ApJS*, 192, 9
- Vigan, A., Fontanive, C., Meyer, M., et al. 2021, *A&A*, 651, A72
- Vorobyov, E. I. 2016, *A&A*, 590, A115
- Wang, P., Li, Z.-Y., Abel, T., & Nakamura, F. 2010, *ApJ*, 709, 27
- Wu, Y.-L., Bowler, B., Sheehan, P. D., et al. 2022, *ApJL*, 930, L3
- Zhou, Y., Sanghi, A., Bowler, B., et al. 2022, *ApJL*, 934, L13
- Zhu, Z., Hartmann, L., & Gammie, C. 2010, *ApJ*, 713, 1143

Table 1. Initial conditions for the models with varied maximum number of refinement levels, initial outer disk and envelope temperatures (K), initial minimum Toomre Q , outer disk radii (au), box size (au), and critical density needed for sink particle formation (cgs).

Model	N_{levels}	T_{disk}	$T_{envelope}$	$Q_{minimum}$	R_{disk}	S_{box}	$\rho_{crit-sinks}$
3-1K-20	3	40	40	1.3	20	60	10^{-8}
4-1K-20	4	40	40	1.3	20	60	10^{-8}
5-1K-20	5	40	40	1.3	20	60	10^{-7}
6-1K-20	6	40	40	1.3	20	60	10^{-7}
3-2K-30	3	80	80	1.9	30	60	10^{-9}
4-2K-30	4	80	80	1.9	30	60	10^{-9}
5-2K-30	5	80	80	1.9	30	60	10^{-9}
6-2K-30	6	80	80	1.9	30	60	10^{-9}
7-2K-30	7	80	80	1.9	30	60	10^{-9}
3-2K-60-11	3	80	120	1.9	60	120	10^{-11}
34-2K-60-11	3-4	80	120	1.9	60	120	10^{-11}
4-2K-60-10	4	80	120	1.9	60	120	10^{-10}
4-2K-60-11	4	80	120	1.9	60	120	10^{-11}
3-3K-60-10	3	120	120	2.2	60	120	10^{-10}
3-3K-60-11	3	120	120	2.2	60	120	10^{-11}
34-3K-60-10	3-4	120	120	2.2	60	120	10^{-10}
34-3K-60-11	3-4	120	120	2.2	60	120	10^{-11}
4-3K-60-10	4	120	120	2.2	60	120	10^{-10}
4-3K-60-11	4	120	120	2.2	60	120	10^{-11}
3-4K-60-10	3	160	120	2.5	60	120	10^{-10}
3-4K-60-11	3	160	120	2.5	60	120	10^{-11}

Table 2. Results for the models, showing the maximum number of sinks formed, final number of sinks, number of times a sink reached escape velocity, number of sinks lost to mergers, and final time (yrs).

Model	$N_{max-sinks}$	$N_{final-sinks}$	$N_{escaped-sinks}$	$N_{merged-sinks}$	t_{final}
3-1K-20	4	2	0	2	2000
4-1K-20	11	3	0	8	2000
5-1K-20	23	11	130	12	2000
6-1K-20	30	18	540	12	2000
3-2K-30	13	2	6	11	2000
4-2K-30	15	3	50	12	2000
5-2K-30	19	5	110	14	2000
6-2K-30	0	0	0	0	326
7-2K-30	0	0	0	0	340
3-2K-60-11	25	4	0	21	1000
34-2K-60-11	12	2	15	10	1000
4-2K-60-10	0	0	0	0	130
4-2K-60-11	0	0	0	0	234
3-3K-60-10	12	2	0	10	1000
3-3K-60-11	11	2	0	9	1000
34-3K-60-10	10	3	0	7	890
34-3K-60-11	10	5	0	5	1000
4-3K-60-10	0	0	0	0	250
4-3K-60-11	0	0	0	0	268
3-4K-60-10	0	0	0	0	86
3-4K-60-11	0	0	0	0	142

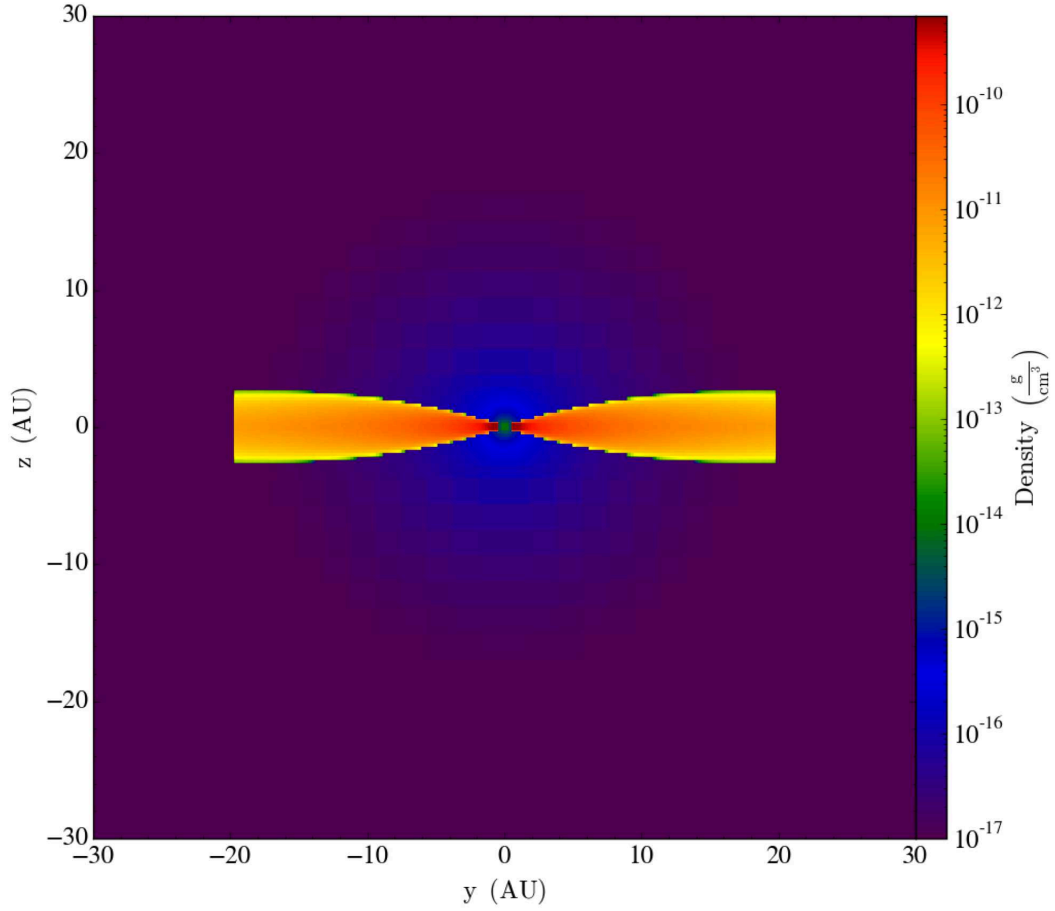


Fig. 1.— Initial log density cross-section in a vertical section ($x = 0$) showing the entire computational grid with a maximum of three levels of refinement for the 20 au outer disk radius models.

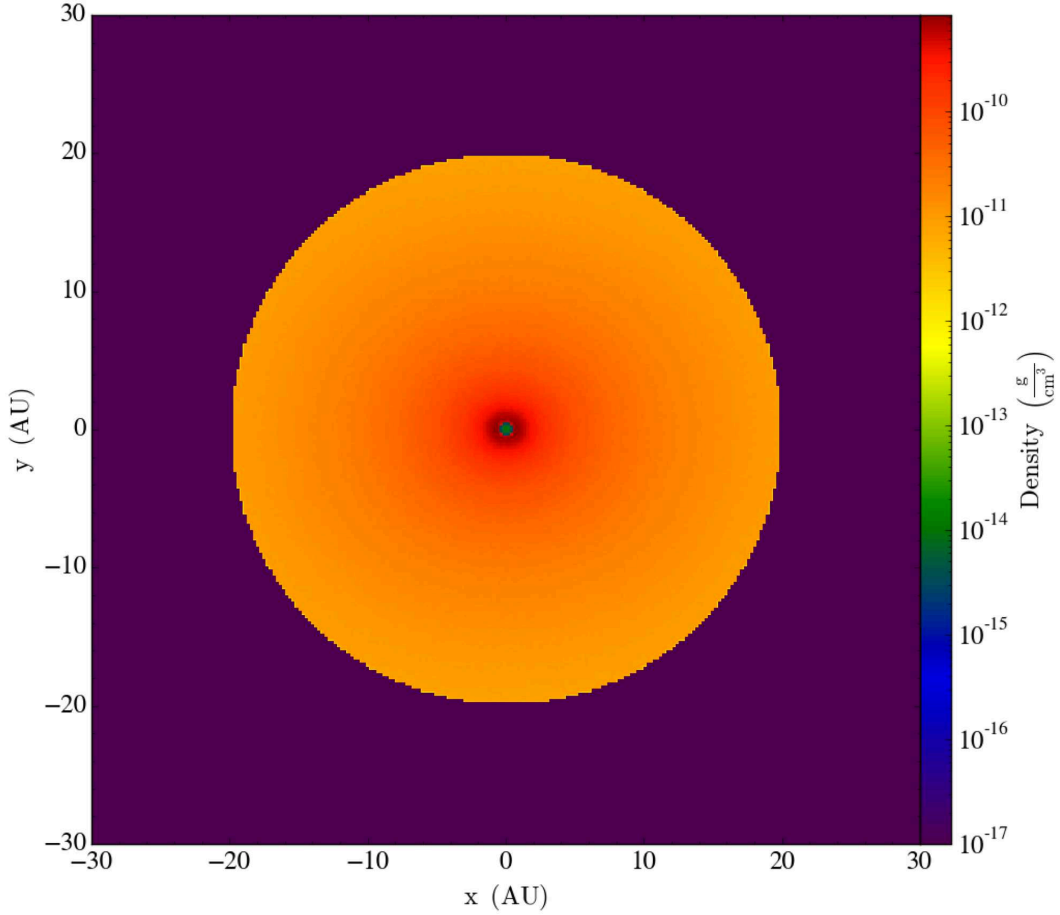


Fig. 2.— Initial log density cross-section in the disk midplane ($z = 0$) showing the entire computational grid with a maximum of three levels of refinement for the 20 au outer disk radius models. With six levels of refinement, the inner 1 au is better resolved, but otherwise the initial disk is identical.

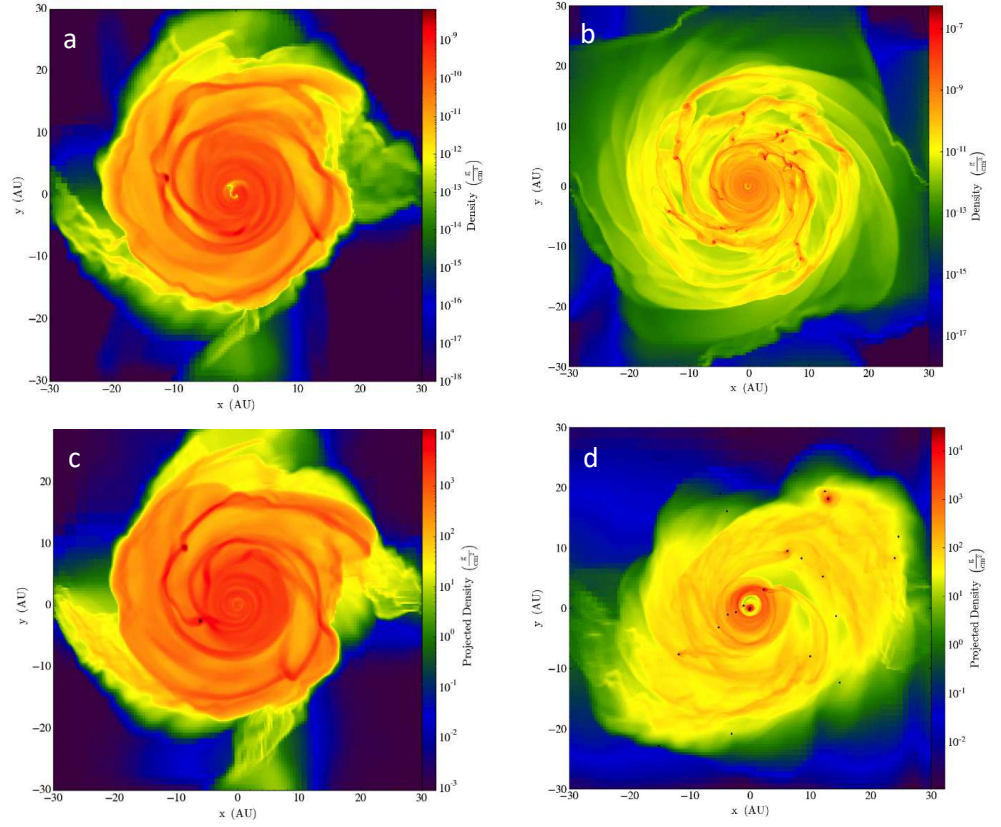


Fig. 3.— Log density cross-section in the disk midplane ($z = 0$) after 190 yr of evolution for model 3-1K-20 without (a) and with (c) sink particles, and model 6-1K-20 without (b) and with (d) sink particles.

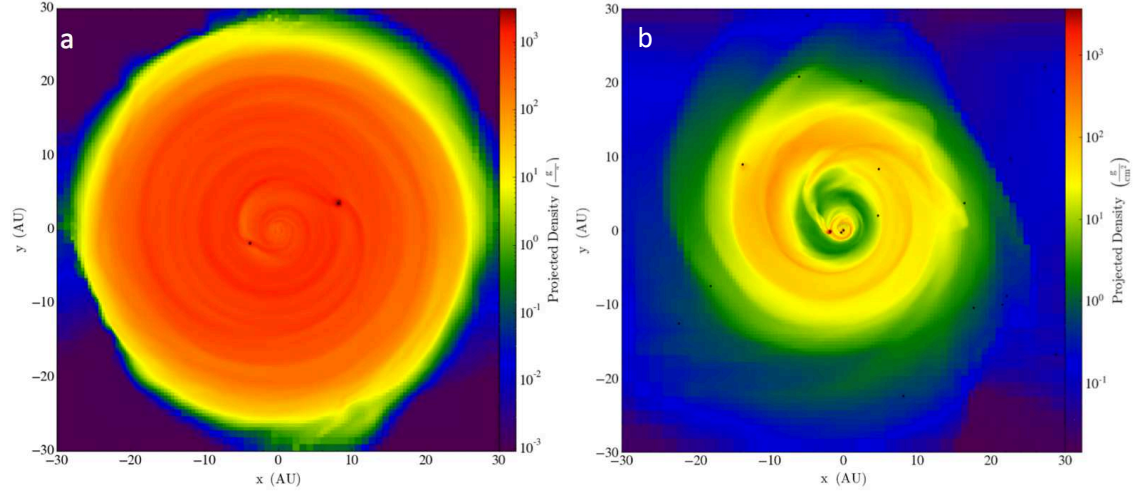


Fig. 4.— Log density cross-section in the disk midplane ($z = 0$) after 2000 yr of evolution for (a) model 3-1K-20 and (b) model 6-1K-20, both with sink particles.

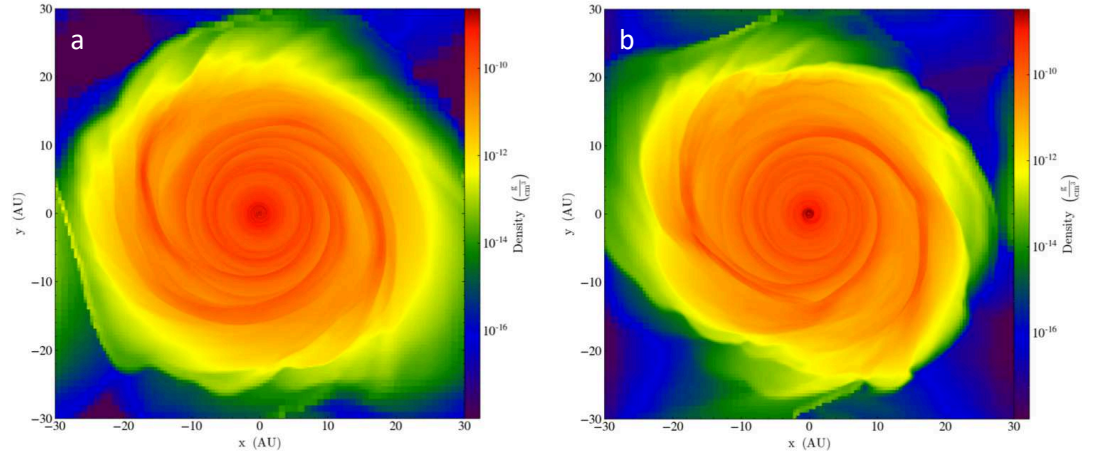


Fig. 5.— Log density cross-section in the disk midplane ($z = 0$) for (a) model 6-2K-30 and (b) model 7-2K-30 after 326 yr and 340 yr of evolution, respectively.

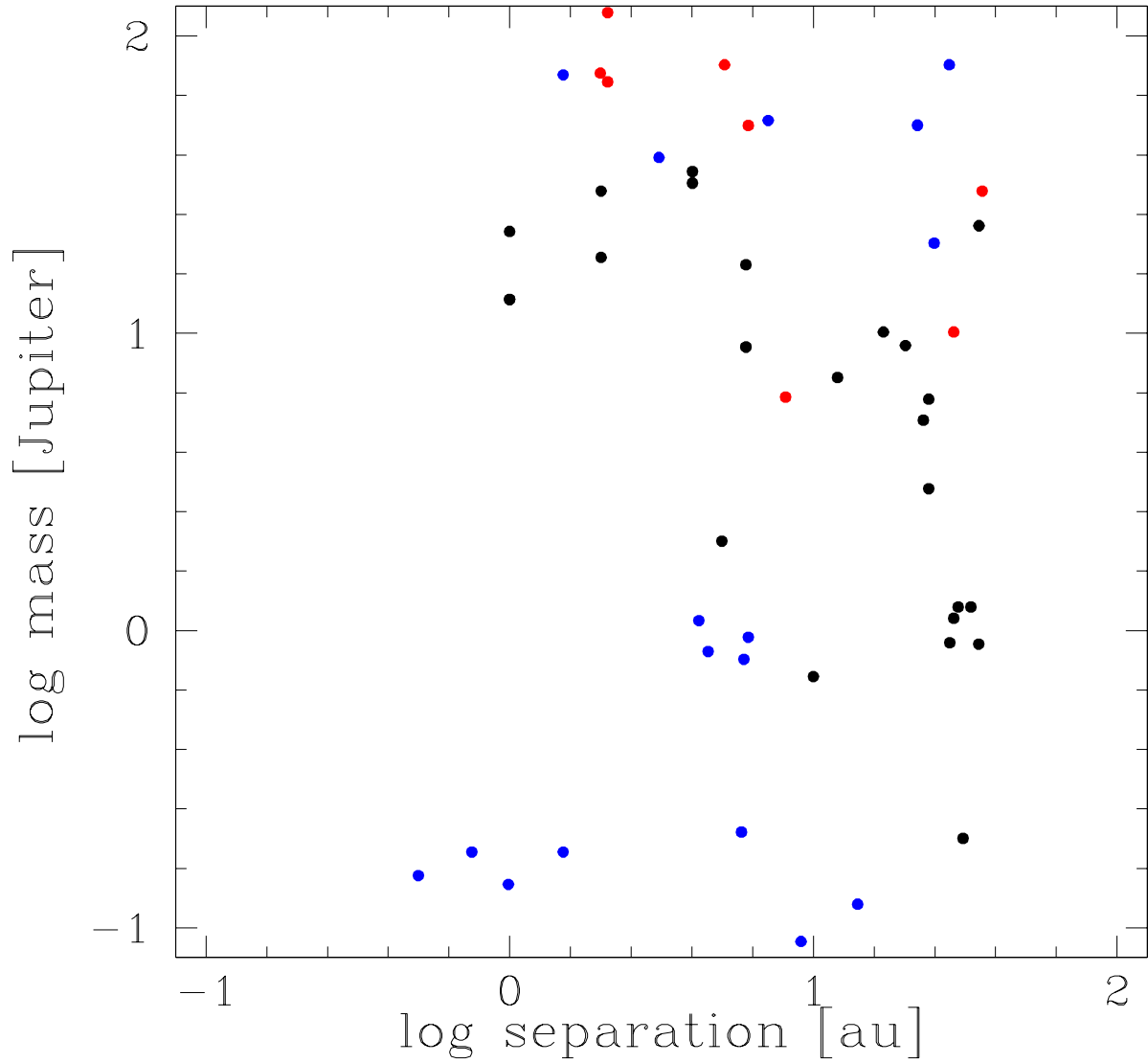


Fig. 6.— Sink particle masses and distances from central star at the final times for the models. These distances correspond to observed separations in the absence of knowledge of the orbital parameters, i.e., the semi-major axis and eccentricity. Black dots are for models that started with 20 au radius disks, red dots are for 30 au disks, and blue dots are for 60 au radius disks (see Table 1).

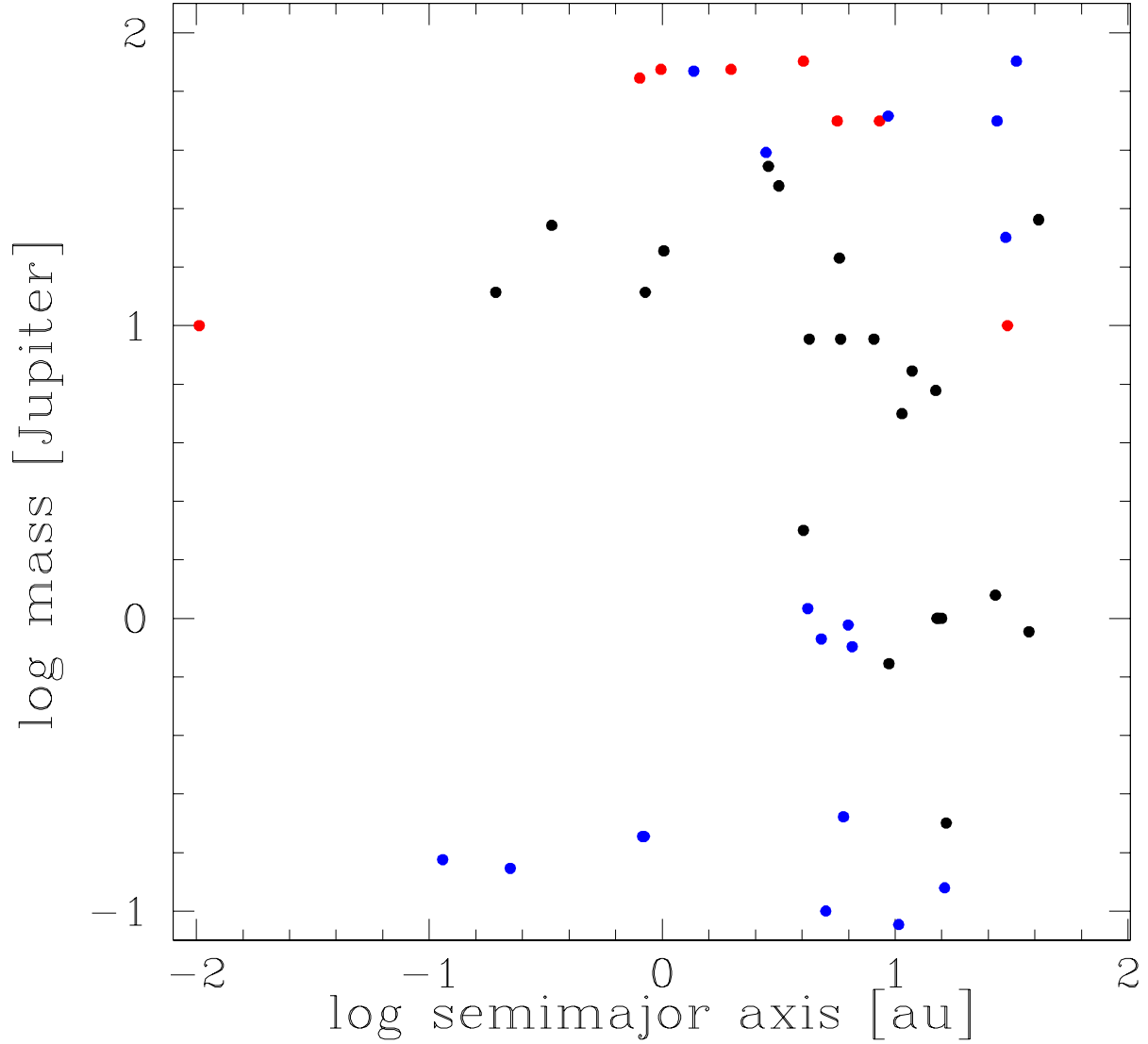


Fig. 7.— Sink particle masses as a function of the orbital semimajor axis at the final times for the models. Black dots are for models that started with 20 au radius disks, red dots are for 30 au disks, and blue dots are for 60 au radius disks (see Table 1).

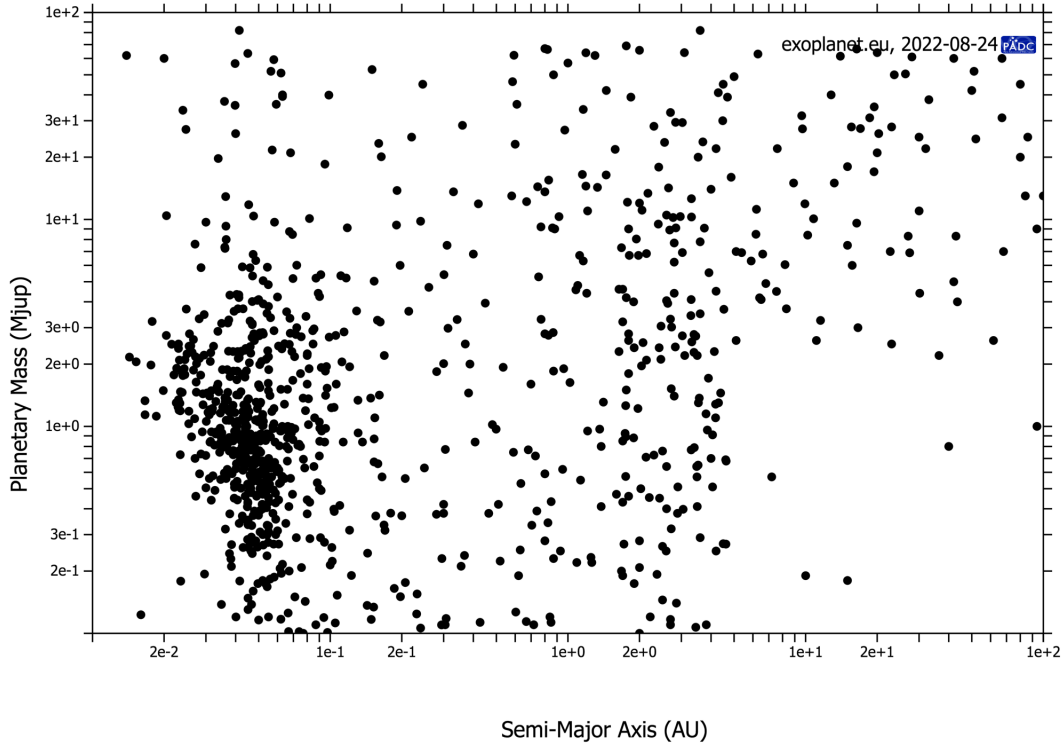


Fig. 8.— Exoplanet masses as a function of orbital semimajor axis from the Extrasolar Planets Encyclopaedia (exoplanet.eu) as of 24 August 2022.

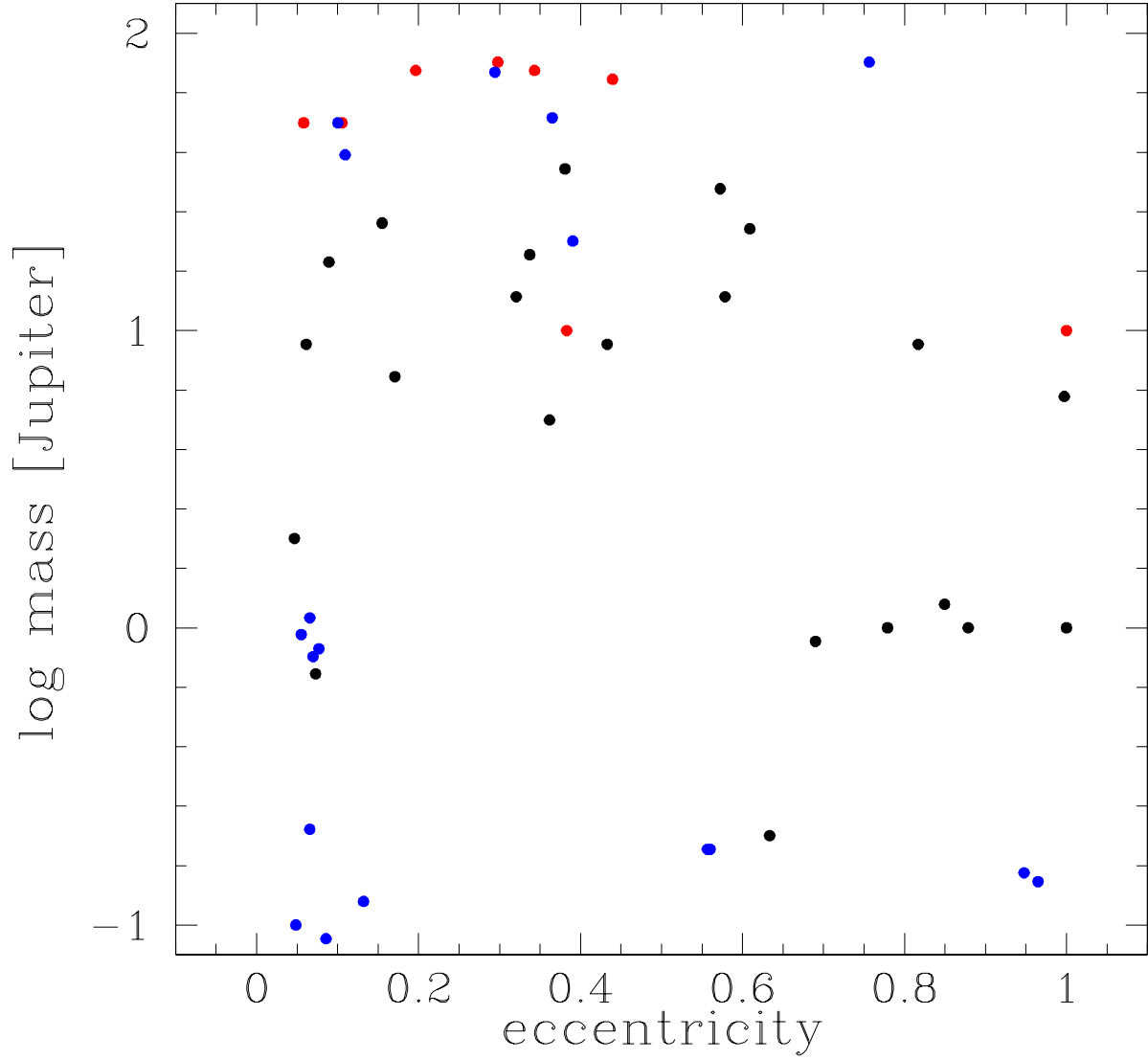


Fig. 9.— Sink particle masses as a function of the orbital eccentricity at the final times for the models. Black dots are for models that started with 20 au radius disks, red dots are for 30 au disks, and blue dots are for 60 au radius disks (see Table 1).

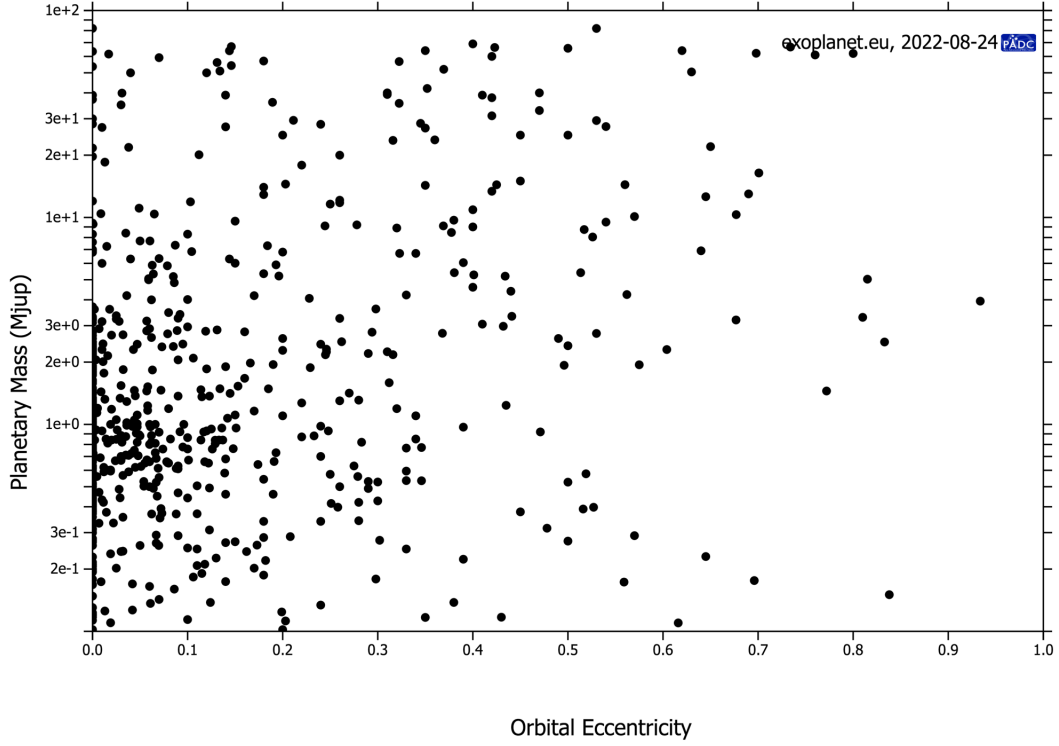


Fig. 10.— Exoplanet masses as a function of orbital eccentricity from the Extrasolar Planets Encyclopaedia (exoplanet.eu) as of 24 August 2022.